Improved differential method for microstructured optical fibres

Philippe Boyer, Gilles Renversez, Evgeny Popov and Michel Nevière

Institut Fresnel (Unité Mixte de Recherche du Centre National de Recherche Scientifique, UMR 6133), Université Paul Cézanne Aix-Marseille III, et Université de Provence, Faculté des Sciences et Techniques de Saint Jérôme, Avenue Escadrille Normandie-Niémen, 13397 Marseille cedex 20, France

E-mail: gilles.renversez@fresnel.fr

Abstract
We describe an improved differential method for calculating the leaky modes of finite size microstructured optical fibres. This method, which includes the fast Fourier factorization method, is used here in cylindrical coordinates. The method utilizes a reformulation of the Maxwell equations in a Fourier space taking into account the Fourier expansion truncations and the possible discontinuities of the permittivity. For waveguides fulfilling C_{nv} symmetries, the symmetry properties of the modes are established in Fourier space for cylindrical coordinates in real space. This result allows us to reduce the required computer resources. The method can deal with arbitrary cross-section microstructured optical fibres made of inhomogeneous inclusions or matrix. We validate the method through several comparisons with the well established multipole method and with other methods. We also illustrate the application of the differential theory to calculate the modal properties of complex microstructured optical fibres that cannot be studied with the multipole method.

1. Introduction

Microstructured optical fibres (MOFs) are now a common research topic in guided optics. Several powerful methods have been developed to study numerically the modal properties of these new devices [1–3]. Nevertheless only a few of them are able to determine the imaginary part of the leaky mode effective index found in MOFs [2, 4, 5]. This quantity is required in order to study the losses of the fundamental mode in finite size microstructured fibre [6, 7] or the transition of the second mode in such structures [8, 9]. The multipole method (MM), which is now used by many research groups across the world to study MOFs, is certainly the fastest and the most precise method when the guiding structure is only made of circular and homogeneous inclusions. In this case, it can be considered as the reference method. However, this well established method has the limitation that the inclusions,

eventually not circular, must be included in non-overlapping circles. This restriction limits the type of MOF profiles which can be studied. A second limitation concerns the matrix, whose refractive index must be constant in the region surrounding the inclusions. These two limitations come from the use of the Graf's theorem that allows us to express the field diffracted by an inclusion as an incoming field on the other inclusions composing the structure [2].

The classic MM has already been extended in order to deal with non-circular inclusions fulfilling the first limitation detailed above [10]. To do so, an improved differential method including the fast Fourier factorization (FFF) [11, 12] has been used to provide the scattering matrix of each non-circular inclusion of the MOF to the MM. In order to overcome simultaneously the two limitations of the MM, extended or not, but keeping as much as possible the accuracy of this method, we used the differential method with the FFF to build

a complete modal method giving directly and accurately the complex effective index of the modes, as the MM does. We recall that the main idea of differential methods is to get a first order differential system instead of the second order one obtained directly from the Maxwell's equations, with the differential system then being solved numerically.

Since the differential method in cylindrical coordinates has already been published for diffraction problems [13], we do not need to repeat its basic concepts. More recently, in a preliminary study, we have proved that this method can be formulated to study modal properties [14]. Nevertheless, due to numerical instabilities, the proposed set of equations does not permit us to study MOFs with an extended microstructured region along the radial variable. Besides, the relations between the modes and the symmetries of the studied MOF were not described in complete detail and only a partial validation of the method was realized. In the present work, all these issues are fully treated in order to give a complete and useful version of the improved differential method with the FFF applied to mode searching in waveguides with discrete symmetries in their cross-section. The purpose of this work is also to demonstrate the accuracy and the versatility of the described method.

In section 2, we recall how we adapt the differential method to modal analysis, and we provide the set of equations which is numerically stable. In section 3, we explain in detail how the possible symmetry properties of the studied waveguide cross-sections are taken into account. In section 4, in order to validate carefully this new method, several comparisons especially with the MM results are made, and the convergence properties according to the different parameters of the method are described. Results that cannot be computed with the MM (extended or not) are given for sectorial inclusion MOFs in section 5, and are compared with those obtained with two other methods. New results for this type of MOFs are also given in this section. Finally, new results are obtained for inhomogeneous MOFs in section 6.

2. An FFF based modal searching method: the FFF-MS

2.1. Mode searching with the differential method

In order to concentrate on the modal problem and to avoid repeating what we have already published in previous articles dedicated to the FFF [13, 14], we refer to these references for the description of the FFF. We simply recall that the key point of the FFF is to rewrite the formulation of the linear relation between **E** and **D** in a truncated Fourier space. We found that, locally [13, 14],

$$[D] = Q_\varepsilon[E] \tag{1}$$

in which the column matrices $[D]$ and $[E]$ are made up of three blocks, each of these blocks (r, θ, z) containing $2N+1$ Fourier components, and Q_ε is a square matrix. The size of this matrix is $3(2N + 1)$ since it comprises the Toeplitz matrices: $[\![n_r^2]\!]$, $[\![n_r n_\theta]\!]$, $[\![n_\theta^2]\!]$, built from the extended unit vectors (denoted by **n**) normal to the surfaces of the inclusions. The matrix Q_ε also contains the Toeplitz matrices $[\![\epsilon]\!]$ and $[\![1/\epsilon]\!]^{-1}$ arising from the application of the correct factorization rules, described by Li [15], used to reformulate the constitutive relation $\mathbf{D} = \epsilon\mathbf{E}$ in

the truncated Fourier space (see section 4.7 of [16] and quoted references for the detailed properties of Toeplitz matrices).

This rewriting of the constitutive relation is used explicitly in a region called the 'modulated area'. This area, which lies between the inscribed circular cylinder $C_{\min}$ with radius $R_{\min}$ and the circumscribed circular cylinder $C_{\max}$ with radius $R_{\max}$, contains all the diffracting cylindrical objects. For MOFs, this region contains the inclusions which confine the electromagnetic fields. In the modulated area, Maxwell's equations are reduced to a set of first order differential equations written in a four block matrix form (one block for each field component used in the theory):

$$\frac{\mathrm{d}}{\mathrm{d}r} \begin{bmatrix} [E_\theta] \\ [E_z] \\ [H_\theta] \\ [H_z] \end{bmatrix} = \mathrm{i}M(r) \begin{bmatrix} [E_\theta] \\ [E_z] \\ [H_\theta] \\ [H_z] \end{bmatrix} \tag{2}$$

in which $M(r)$ is a square matrix, depending on the blocks of the matrix Q_ε, with dimension $4(2N + 1)$ and whose general expression valid for anisotropic, lossless or lossy, and/or inhomogeneous media can be found in [13]. A simplified expression of $M(r)$ for the present case (z-invariance and isotropic medium) can be found in [14].

2.2. First approach

Modes are homogeneous solutions of Maxwell's equations, of the form $f(r, \theta) \exp(\mathrm{i}(\beta z - \omega t))$, in which β is the modal propagation constant and ω is the angular frequency.

In a homogeneous and isotropic medium, the Fourier coefficients of the electromagnetic field components, $E_{z,n}$ and $H_{z,n}$, satisfy the following propagation equation, written in cylindrical coordinates:

$$\left(k_{t,j}r\right)^2 \frac{\mathrm{d}^2 u_{z,n}}{\mathrm{d}\left(k_{t,j}r\right)^2} + \left(k_{t,j}r\right)\frac{\mathrm{d}u_{z,n}}{\mathrm{d}\left(k_{t,j}r\right)} + \left[\left(k_{t,j}r\right)^2 - n^2\right] u_{z,n} = 0 \tag{3}$$

with $u_{z,n} \in \{E_{z,n}, H_{z,n}\}$, $k_{t,j}^2 = k_j^2 - \beta^2$, $k_j^2 = \omega^2\mu_0\epsilon_j$, and $j \in \{\text{int}, \text{ext}\}$. The solutions are

$$\begin{aligned} H_{z,n} &= A_{h,n}^{(j)} J_n\left(k_{t,j}r\right) + B_{h,n}^{(j)} H_n^+\left(k_{t,j}r\right) \\ E_{z,n} &= A_{e,n}^{(j)} J_n\left(k_{t,j}r\right) + B_{e,n}^{(j)} H_n^+\left(k_{t,j}r\right). \end{aligned} \tag{4}$$

In order to simplify the equations, we introduce the following column matrices with dimension $2(2N + 1)$:

$$[A(r)] = \begin{bmatrix} \vdots \\ A_{e,n}^{(j)} J_n\left(k_{t,j}r\right) \\ \vdots \\ A_{h,n}^{(j)} J_n\left(k_{t,j}r\right) \\ \vdots \end{bmatrix} \quad \text{and}$$

$$[B(r)] = \begin{bmatrix} \vdots \\ B_{e,n}^{(j)} H_n^+\left(k_{t,j}r\right) \\ \vdots \\ B_{h,n}^{(j)} H_n^+\left(k_{t,j}r\right) \\ \vdots \end{bmatrix}. \tag{5}$$

We have omitted the j superscript in the left-hand sides of equations (5). We recall that at $r = R_{\min}$, $j = \text{int}$, and at $r = R_{\max}$, $j = \text{ext}$. The scattering matrix S of the entire modulated area is defined by

$$\begin{bmatrix} [B(R_{\max})] \\ [A(R_{\min})] \end{bmatrix} = S \begin{bmatrix} [B(R_{\min})] \\ [A(R_{\max})] \end{bmatrix}$$
$$= \begin{bmatrix} S_{11} & S_{12} \\ S_{21} & S_{22} \end{bmatrix} \begin{bmatrix} [B(R_{\min})] \\ [A(R_{\max})] \end{bmatrix}. \quad (6)$$

To avoid a divergence of the field at the origin ($H_n^+(r) \to \infty$ when $r \to 0$) we must have $B_{e,n}^{(\text{int})} = 0$ and $B_{h,n}^{(\text{int})} = 0 \, \forall n$, i.e. $[B(R_{\min})] = [0]$. In the external region, the amplitudes $B_{e,n}^{(\text{ext})}$ and $B_{h,n}^{(\text{ext})}$, which are the coefficients of Hankel functions, are associated with outgoing waves, whereas the amplitudes $A_{e,n}^{(\text{ext})}$ and $A_{h,n}^{(\text{ext})}$, which are the multiplicative coefficients of Bessel functions, are associated with incident waves. Then, recalling that modes are homogeneous solutions of Maxwell's equations, we must have $A_{e,n}^{(\text{ext})} = 0$ and $A_{h,n}^{(\text{ext})} = 0 \, \forall n$, i.e. $[A(R_{\max})] = [0]$. Using equation (6), we obtain that, for modal fields, the column matrices $[A(R_{\min})]$ and $[B(R_{\max})]$ must be solutions of the following homogeneous set of equations:

$$S^{-1} \begin{bmatrix} [B(R_{\max})] \\ [A(R_{\min})] \end{bmatrix} = \begin{bmatrix} 0 \\ 0 \end{bmatrix}. \quad (7)$$

Thus, the unknown amplitudes appear to be the eigenvectors associated with null eigenvalues of the inverse scattering matrix S^{-1}. Once determined, equation (4) allows us to compute the fields.

2.3. Improved approach in the S-matrix propagation algorithm with the Z-matrix

In most cases, numerical instabilities do not permit us to integrate the differential set (2) directly from $r = R_{\min}$ to $r = R_{\max}$; this is why we use the S-matrix propagation algorithm [11]. In fact, for a fixed value of the argument $k_{t,\text{int}} R_{\min}$ (see equation (4)), the spatial extension of the divergence due to the singularity of the Hankel functions at $r = 0$ spreads out along the r axis when the Bessel order n increases towards its maximum value fixed by the truncation order N. Consequently, the initial vectors of the integration evaluated at $r = R_{\min}$ and calculated from equation (34) of [13] may contain high values which grow during the integration process and can make some blocks of the transmission matrix T ill conditioned. We remind the reader that the T-matrix links the fields at $r = R_{\min}$ and the fields at $r = R_{\max}$. In order to avoid this numerical contamination, the principle of the S-matrix propagation algorithm is to split the modulated area into L slices. For each slice (s) limited by the circular cylinders with radius r_s and r_{s+1} ($r_1 = R_{\min}$ and $r_{L+1} = R_{\max}$), the differential set (2) is integrated. At $r = r_s$ for $s \in [2, L]$, we add for each interface an infinite thin homogeneous layer with permittivity ϵ_{ext}. Consequently, the column matrices defined by expression (5) can be generalized to the interfaces within the modulated area (see also figure 6 of [13]). We obtain the corresponding T-matrix denoted $T^{(s)}$ of the (s) slice which links the fields at r_s and the fields at r_{s+1}. We use the S-matrix of the (s) interface $r = r_s$, denoted $S^{(s)}$, and fully defined in equation (40) of [13]. The S-matrix $S^{(s)}$ was defined in order

to be better conditioned than the T-matrix $T^{(s)}$. We recall that the S_{22} block is such that

$$S_{22}^{(s+1)} = S_{22}^{(s)} Z^{(s)} \quad (8)$$

with

$$Z^{(s)} = \{T_{11}^{(s)} + T_{12}^{(s)} S_{12}^{(s)}\}^{-1}. \quad (9)$$

At the end of the S-matrix propagation algorithm process, we obtain the S-matrix at the $(L + 1)$ interface. This matrix is simply the required S-matrix associated with the whole modulated area (see equation (6)).

The modal problem initially described by equation (7), with the large $4(2N + 1)$ square matrix S^{-1}, may be performed using the benefits of the S-matrix propagation algorithm. From equation (8), we deduce $\{S_{22}^{(s)}\}^{-1} = Z^{(s)} \{S_{22}^{(s+1)}\}^{-1}$. Then we multiply each side by the same vector $[A(R_{\min})]$:

$$\{S_{22}^{(s)}\}^{-1} [A(R_{\min})] = Z^{(s)} \{S_{22}^{(s+1)}\}^{-1} [A(R_{\min})]. \quad (10)$$

Using equation (40) of [13] and identifying the left- and right-hand terms in equation (10), we obtain

$$[A(r_s)] = Z^{(s)} [A(r_{s+1})]. \quad (11)$$

In order to complete the field expansion at the interface r_s, we use again equation (40) of [13], and we get

$$[B(r_s)] = S_{12}^{(s)} [A(r_s)]. \quad (12)$$

For the Lth slice, using equation (11) we note that the modal fields at the Lth interface are a solution of

$$[A(r_L)] = Z^{(L)} [0] \qquad \text{or equivalently} \qquad (13)$$

$$\{Z^{(L)}\}^{-1} [A(r_L)] = [0] \quad (14)$$

and the fields at the other interfaces are deduced through an iterative method by equations (11) and (12).

Equation (14) is a new formulation of the modal problem. Solving this equation presents two important advantages. First, the block $\{Z^{(L)}\}^{-1} = T_{11}^{(L)} + T_{12}^{(L)} S_{12}^{(L)}$ (see equation (9)) is well conditioned by definition if the number of slices in the S-matrix propagation algorithm is sufficient. The $\{Z^{(L)}\}^{-1}$-matrix is better conditioned than the S^{-1}-matrix and its size is halved. These properties allow us to study waveguides with a microstructured region, i.e. a modulated region in the FFF terminology, more extended along the r variable than the simple formulation we proposed previously [14]. We illustrate this improvement in section 4.1. We can note that, as in section 2.2, the fields can be computed in the entire device cross-section from the eigenvectors of the $\{Z^{(L)}\}^{-1}$-matrix associated with a null eigenvalue using equations (11) and (12). In what follows, we will simply denote the $\{Z^{(L)}\}^{-1}$-matrix by Z^{-1} and we will denote the FFF based mode searching method that we develop the FFF-MS.

The search algorithm we use within the FFF-MS is similar to the one detailed in chapter 5 of [2]. However, since the computation of the S^{-1} scattering matrix of the whole MOF is more time consuming with this method than with the MM, we reduce as much as possible the number of evaluations of the Z^{-1}-matrix, even if this slightly reduces the capability of the algorithm to find automatically the modes of a given structure.

3. Modes and symmetries

3.1. Device with sub-periodicity according to the angular variable θ

Typical MOF cross-sections often have a sub-periodicity with respect to the angular variable θ, at least as a first approximation. Nearly all the MOFs already realized fulfil the C_{nv} symmetry, i.e. a sub-periodicity of $2\pi/n$ with symmetry planes ($n \in \mathbb{N}^*$); most of them belong to the C_{6v} one. This property and the useful and general work of McIsaac [17, 18] relating waveguide symmetry properties and mode classification, using a group-theoretic approach, have already motivated the exploitation of the putative sub-periodicity according to θ. To use the symmetry properties of the structures studied has the following advantages: it allows a clear mode classification according to McIsaac's results. In addition, by reducing the size of the matrices in the numerical implementation of the method, it reduces the computation time and it avoids the loss of accuracy induced by the increase of the number of numerical operations when the matrix size is increased. For the already mentioned multipole method, all these benefits have already been obtained [6, 2, 19]. It is then obvious that such an improvement should be obtained in the framework of the FFF-MS. It is worth mentioning that both the MM and finite element method [2] deal with real space. Consequently, the symmetry relations are defined and used in this space. Bai and Li have established a formulation of the differential method for diffraction problems of crossed gratings using Cartesian coordinates using the structure symmetries [20, 21]. In our work, the FFF method is formulated in the Fourier space for cylindrical coordinates (see section 3 of [13]), and symmetry properties have to be found in the Fourier space using angular periodicities of microstructured optical fibres.

The sub-periodicity in θ directly implies some properties for the Fourier expansions of the optogeometric quantities ($\bar{\bar{\epsilon}}, n_r, n_\theta, \ldots$) used by the FFF, and then induces a splitting of the differential set into several independent sub-sets as we show in the following.

First, let us define the Fourier expansion of a geometrical quantity denoted $w(\theta)$ with sub-period T such that $N_T T = 2\pi$ where N_T is the sub-periodicity number (for a C_{6v} structure, we have $N_T = 6$). On the 2π-period, the Fourier expansion of $w(\theta)$ is written

$$w(\theta) = \sum_{n=-\infty}^{\infty} w_n e^{in\theta} \qquad \text{with } w_n = \frac{1}{2\pi} \int_0^{2\pi} w(\theta) e^{-in\theta} \, d\theta. \tag{15}$$

The Fourier expansion of $w(\theta)$ on the sub-period T is written

$$w(\theta) = \sum_{n=-\infty}^{\infty} w'_n e^{in\frac{2\pi}{T}\theta}$$

$$\text{with } w'_n = \frac{1}{T} \int_0^T w(\theta) e^{-in\frac{2\pi}{T}\theta} \, d\theta. \tag{16}$$

After a few calculations, we obtain the known result:

$$\rightarrow \forall n \in \mathbb{Z}, \begin{cases} \text{if } n \neq mN_T, m \in \mathbb{Z} \text{ then } w_n = 0, \\ \text{if } n = mN_T, m \in \mathbb{Z} \text{ then } w_n = w_{mN_T} = w'_m. \end{cases} \tag{17}$$

The Fourier spectrum of $w(\theta)$ on the 2π-range is the Fourier spectrum of $w(\theta)$ on the sub-period T with an enlargement of factor N_T. Let us illustrate the consequences of this property (17) on a simple example in which $N_T = 3$. The Fourier coefficients of $w(\theta)$ in the T-range (w'_n) are $\{\ldots, w'_{-4}, w'_{-3}, w'_{-2}, w'_{-1}, w'_0, w'_1, w'_2, w'_3, w'_4, \ldots\}$ and, according to the property (17), the Fourier coefficients of w on the 2π-range (w_n) are $\{\ldots, 0, 0, w'_{-2}, 0, 0, w'_{-1}, 0, 0, w'_0, 0, 0, w'_1, 0, 0, w'_2, 0, 0, \ldots\}$. Consequently, the Toeplitz matrix of $w(\theta)$ denoted $[\![w]\!]$ (see section 4.7 of [16] and quoted references for the detailed properties of Toeplitz matrices) on the 2π-period contains non-null diagonals regularly separated by ($N_T - 1$) null diagonals.

Moreover, when we invert such a matrix, such as $[\![w]\!]$, or multiply two such matrices, the matrix structure is preserved even if the matrix obtained is not usually a Toeplitz matrix.

The blocks of the integration matrix $M(r)$ in equation (2) are not Toeplitz matrices since some of them contain the matrix α and the blocks of the matrix Q_ϵ [13]; nevertheless, these blocks keep the diagonal structure of the matrix $[\![w]\!]$. Consequently, the differential set (2) is split into $N_T = 3$ independent differential sub-sets which link the Fourier coefficients of the field components (E_θ, E_z, H_θ or H_z) among the following classes of expansion orders: $\{-4, -1, 2\}$, $\{-3, 0, 3\}$ and $\{-2, 1, 4\}$.

To conclude, when we consider a sub-periodicity with N_T sub-periods, the differential set (2) is split into N_T independent and different sub-sets. However each block of the Q_ϵ-matrix contains the same terms for all the differential sub-sets. The computational time depends approximatively on the cube of the matrix integration size, equal to $4(2N + 1)$, whereas the size of the integration matrix of each sub-set is $4(2N + 1)/N_T$ or less. So the duration of an integration for all the differential sub-sets scales as $N_T(4(2N + 1)/N_T)^3 = (4(2N + 1))^3/N_T^2$, while the computational time of the global differential set scales as $(4(2N + 1))^3$. Hence taking into account the sub-periodicity permits us to reduce approximatively the computation time by a factor of N_T^2 (36 for a C_{6v} structure).

3.2. Using the mode symmetries within the FFF-MS

In section 3.1, we have shown that the sub-periodicities imply the splitting of the Fourier coefficient set of the modal electromagnetic fields into N_T independent sub-sets, all these sub-sets being required to compute the modal fields. In the present section, we first show that it is sufficient to study one or two sub-sets to describe completely the modal field of a $C_{N_T v}$ structures. This result is related to the exhaustive description of symmetry classes and field expressions of waveguide modes established by McIsaac [17, 18] and improved by Fini [19]. Secondly, we explain explicitly how the modal fields (Fourier amplitudes) are computed in the FFF-MS using the improved approach in the S-matrix propagation algorithm.

For a sub-periodicity order N_T, we choose to denote by I_i the N_T sub-sets of Fourier coefficient orders in the following way:

$$I_i = \{nN_T + i - 1, n \in \mathbb{Z}\} \qquad \text{with } i \in [1, N_T]. \tag{18}$$

We only consider a $C_{N_T v}$ symmetry MOF; the C_{N_T} case can be found in a similar way. When N_T is odd, we know

Table 1. Fourier series representations of the longitudinal electric field for waveguides with $C_{N_T v}$ symmetry (the first three columns come from table IV in [17]). As in this reference, the q subscript indicates the qth mode of the considered mode class. See equation (18) for the definition of the I_i.

N_T	Mode class p	E_{zpq}	FFF-MS Fourier coefficients sub-sets
Even, odd	1	$\sum_{n=0}^{n=+\infty} F_{1qn}(r) \cos(N_T n\theta)$	I_1
Even, odd	2	$\sum_{n=0}^{n=+\infty} G_{1qn}(r) \sin(N_T n\theta)$	I_1
Even, odd	k	$\sum_{n=0}^{n=+\infty} \left\{ F_{kqn}(r) \cos\left[\left(N_T n - \frac{k-1}{2}\right)\theta\right] + P_{kqn}(r) \cos\left[\left(N_T n + \frac{k-1}{2}\right)\theta\right]\right\}$	$I_{\frac{1+k}{2}}, I_{N_T + \frac{3-k}{2}}$
Even, odd	$k+1$	$\sum_{n=0}^{n=+\infty} \left\{ G_{(k+1)qn}(r) \sin\left[\left(N_T n - \frac{k-1}{2}\right)\theta\right] + R_{(k+1)qn}(r) \sin\left[\left(N_T n + \frac{k-1}{2}\right)\theta\right]\right\}$	$I_{\frac{1+k}{2}}, I_{N_T + \frac{3-k}{2}}$
Even	$N_T + 1$	$\sum_{n=0}^{n=+\infty} F_{(N_T+1)qn}(r) \cos\left[N_T\left(n + \frac{1}{2}\right)\theta\right]$	$I_{1+\frac{N_T}{2}}$
Even	$N_T + 2$	$\sum_{n=0}^{n=+\infty} G_{(N_T+2)qn}(r) \sin\left[N_T\left(n + \frac{1}{2}\right)\theta\right]$	$I_{1+\frac{N_T}{2}}$

Table 2. Sub-sets of the Fourier coefficients in the FFF-MS associated with the different mode classes as defined by McIsaac for a $C_{N_T v}$ waveguide for several values of N_T.

Mode class p	N_T							
	1	2	3	4	5	6	7	8
1	I_1	I_1	I_1	I_1	I_1	I_1	I_1	I_1
2	I_1	I_1	I_1	I_1	I_1	I_1	I_1	I_1
3	—	I_2	I_2, I_3	I_2, I_4	I_2, I_5	I_2, I_6	I_2, I_7	I_2, I_8
4	—	I_2	I_2, I_3	I_2, I_4	I_2, I_5	I_2, I_6	I_2, I_7	I_2, I_8
5	—	—	—	I_3	I_3, I_4	I_3, I_5	I_3, I_6	I_3, I_7
6	—	—	—	I_3	I_3, I_4	I_3, I_5	I_3, I_6	I_3, I_7
7	—	—	—	—	—	I_4	I_4, I_5	I_4, I_6
8	—	—	—	—	—	I_4	I_4, I_5	I_4, I_6
9	—	—	—	—	—	—	—	I_5
10	—	—	—	—	—	—	—	I_5

from McIsaac's work that there are $N_T + 1$ mode classes. The number of non-degenerate mode classes is equal to two and the number of pairs of twofold degenerate mode classes is $(N_T - 1)/2$. When N_T is even, the number of non-degenerate mode classes is equal to four and the number of pairs of twofold degenerate mode classes is the same $((N_T - 2)/2)$. We complete the three first columns given in table IV of [17] with the sub-sets of Fourier coefficients needed to describe the fields in the FFF-MS for each mode class (see table 1). We notice that some mode classes (C_k and C_{k+1}) need two sub-sets of Fourier coefficients. In table 2, we illustrate the splitting of the Fourier coefficients into sub-sets for a $C_{N_T v}$ symmetry waveguide for N_T from 1 to 8.

In the previous paragraph, we determine the FFF-MS sub-sets of Fourier coefficients that describe each mode class for $C_{N_T v}$ waveguides. Now, we express the Fourier amplitudes of the FFF-MS modal fields w'_n given by equation (16) by comparison with the Fourier expansion expressions given by the third column of table 1, distinguishing non-degenerate mode classes and degenerate mode classes. For a $C_{N_T v}$ symmetry waveguide, we notice that a couple of successive mode classes ($p = 1$ and 2; k and $k + 1$; $N_T + 1$ and $N_T + 2$) need the same FFF-MS Fourier coefficient sub-sets (for example I_1 for $p = 1$ and 2). Thus, we limit the following discussion to even values of N_T; the odd case can be deduced immediately by eliminating the mode classes N_{T+1} and N_{T+2}.

Field expansions in table 1 are expressed in a cosine or sine function basis ($\cos(N_T n\theta)$ and $\sin(N_T n\theta)$), and the Fourier amplitudes $F_{pqn}(r)$, $G_{pqn}(r)$, $P_{pqn}(r)$, and $R_{pqn}(r)$ are real numbers. Using the Euler formula, we find the Fourier expansion of the FFF-MS expressed on the exponential function basis ($e^{iN_T n\theta}$) in equation (16) and the corresponding Fourier amplitudes (w'_n) are complex numbers. Consequently, we deduce from the cosine function that Fourier amplitudes $F_{pqn}(r)$ and $P_{pqn}(r)$ satisfy $w'_{-m} = w'_m$ with $m \geqslant 0$ for mode classes $p = 1$, k and $N_T + 1$, and we deduce from the sine function that Fourier amplitudes $G_{pqn}(r)$ and $R_{pqn}(r)$ satisfy $w'_{-m} = -w'_m$ with $m \geqslant 0$ for mode classes $p = 2$, $k + 1$ and $N_T + 2$.

Now we can come back to the link between the Z-matrix and the above results. We start with the two pairs of non-degenerate mode classes ($p = 1$ and 2; $N_T + 1$ and $N_T + 2$). The determinant map of the Z^{-1} sub-matrix associated with the sub-sets (I_1 or $I_{1+\frac{N_T}{2}}$) provides the effective index of both mode classes. On one hand, the modal fields (i.e. the eigenvectors associated with a null eigenvalue, see equation (14)) corresponding to a Fourier expansion expressed only with cosine functions (mode classes $p = 1$ and $N_T + 1$) contain Fourier amplitudes with identical signs as shown above. On the other hand, the modal fields corresponding to a Fourier expansion expressed only with sine functions (mode classes $p = 2$ and $N_T + 2$) contain Fourier amplitudes with opposite signs.

We now consider the case of degenerate mode classes ($p = k$ and $k + 1$): the determinant map of the Z^{-1} sub-matrix associated with the sub-sets ($I_{\frac{1+k}{2}}$ or $I_{N_T + \frac{3-k}{2}}$) provides the same effective index. The Fourier coefficients of the modal fields are linear combinations of eigenvectors (associated with a null eigenvalue) of the Z^{-1} sub-matrix corresponding to the subsets $I_{\frac{1+k}{2}}$ and $I_{N_T + \frac{3-k}{2}}$. Before combining the eigenvectors, we must normalize them. We choose to normalize through the value of the smallest order Fourier coefficient. The linear combination becomes a summation when the Fourier expansions are expressed with a cosine function (mode class $p = k$) and a difference when the Fourier expansions are expressed with a sine function (mode class $p = k + 1$).

As an example, we consider a waveguide with C_{6v} symmetry (column for $N_T = 6$ in table 2). The Fourier expansion of E_{zpq} is written for the mode class $p = 1$ (first
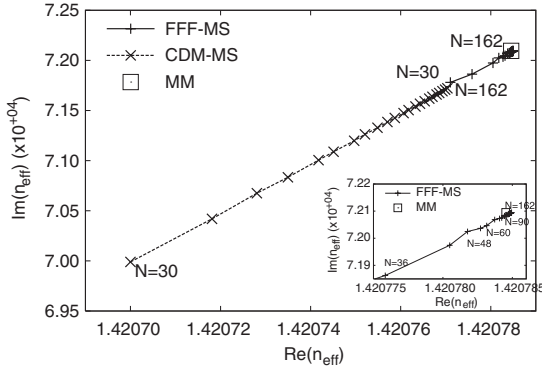
Figure 1. Convergence tests for the FFF-MS and CDM-MS for the effective index of the fundamental mode of the C_{6v} one-ring test MOF described in the text versus the Fourier expansion order N. Inset: zoom of FFF-MS results and MM value.
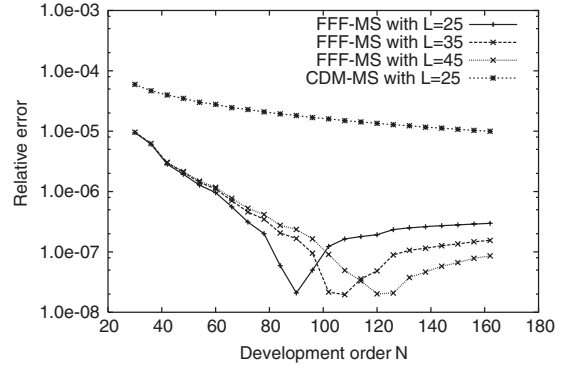

Figure 2. Modulus of the relative difference between the effective indices n_{eff} computed with the FFF-MS for 25, 35 and 45 slices in the S-algorithm, and with the MM result, versus the Fourier expansion order N (for the MM the number of Fourier–Bessel coefficients is equal to 12).

line of table 1):

$$E_{z1q} = \sum_{n=0}^{+\infty} F_{1qn}(r) \cos(6n\theta). \tag{19}$$

Identifying with equation (16), we finally obtain

$$E_{z1q} = \sum_{n=-\infty}^{+\infty} w'_n e^{i6n\theta}$$

with $w'_m = w'_{-m} = \dfrac{F_{1qm}(r)}{2}$ $(m \geqslant 0)$. (20)

The eigenvector deduced from the equation (14) and corresponding to the sub-set I_1 contains these Fourier coefficients w'_n. We can compute the E_{zpq} Fourier expansion for the other mode classes in the same way.

4. Validation of the FFF-MS by comparison with the MM results

In order to validate the FFF-MS as a modal method for studying MOFs we use the MM as a reference method since it is the most accurate method currently available in the case of circular and homogeneous inclusions due to the fact that it is then partially analytic [2]. Our first test system is the C_{6v}, one-ring solid core MOF described in [2]; the hole diameter d is equal to 1 μm, the pitch Λ is equal to 2.3 μm, the matrix index $n_{mat} = 1.443\,903\,5654$ (the number of significant digits given here has no relation to the accuracy with which the refractive index of silica is known at that wavelength; the given values are the ones used in the numerical simulations) and the cylinder index $n_{cyl} = 1$. The second test structure is a C_{2v} six-hole solid core MOF. It is worth mentioning that all the results computed with the FFF shown in this section and the following ones are obtained on a desktop computer with reasonable computation times.

4.1. A C_{6v} MOF

The MM finds an effective index value n_{eff} for the fundamental mode such that $n_{eff} = 1.420\,7845 + i\,7.209\,52 \times 10^{-4}$ for $\lambda = 1.56$ μm for a value of the parameter M, which controls the number of coefficients in the Fourier–Bessel expansion,

equal to 12 (i.e. $2M + 1$ coefficients). For $N = 60$, our mode searching algorithm finds $n_{eff} = 1.420\,783\,15 + i\,7.204\,65 \times 10^{-4}$. In this case the relative error between FFF-MS and MM for the effective index modulus is around 10^{-6}. We test the convergence capability of the FFF-MS according to the Fourier expansion of order N; this is done in figure 1 for the fundamental mode of our test structure. If the correct factorization rules used for the description of the constitutive relation linking **E** and **D** are not included, we are no longer in the frame of the FFF but within the classical differential method (CDM) [22]. It has already been shown that in this case the convergence is much slower and even not attainable (see figures 6 and 10 of [12]) for diffraction problems in TM polarization. The results shown in figure 1 clearly demonstrate that the effective index computed using the FFF-MS converges toward the value obtained from the MM when the Fourier expansion order N is increased. As expected, we can also state that, in a modal problem, the FFF-MS convergence is much faster than the one of the similar mode searching method based on the classical differential method (denoted CDM-MS below).

In order to quantify these convergences, we compute the relative error between the FFF-MS results and the MM ones and also the relative error between the CDM-MS and the MM results. Since n_{eff} is a complex number we use the normalized modulus of the difference between the two values. As can be seen in figure 2, as soon as $N = 60$, the relative error for the FFF-MS is around 10^{-6} for $N = 60$ and reduces to 3×10^{-7} for $N = 162$. The fall of the relative error obtained for 35 slices in the S-matrix propagation algorithm between $N = 84$ and N about 100 is due to the FFF-MS values crossing the MM value. This fall shows that only the global behaviour of the convergence curves must be considered. The field maps of the fundamental mode found with the FFF-MS naturally fulfil the symmetry properties (see section 3.1) as shown in figure 3, and these maps are identical to those obtained with the MM.

Since we have solved the issue of the numerical instabilities occurring in the previous formulation of the FFF-MS applied to mode searching [14], we can now study structures with more than one ring of inclusions, as is proven below. For a two-ring MOF with the same optogeometric parameters as the one-ring MOF described above, the MM
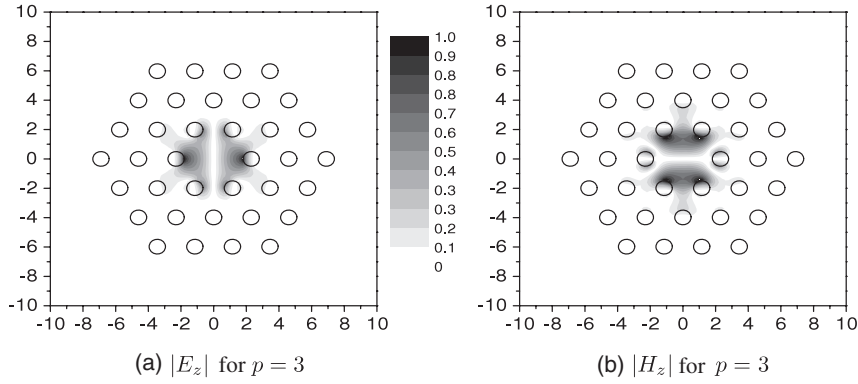
733

(a) $|E_z|$ for $p = 3$

(b) $|H_z|$ for $p = 3$

Figure 3. Moduli of electromagnetic field longitudinal components, in the core region for the degenerate fundamental mode which belongs to symmetry class $p = 3$, $n_{eff} = 1.421\,0465 + i\,8.117 \times 10^{-7}$ for $N = 150$. The field moduli are normalized to unity.
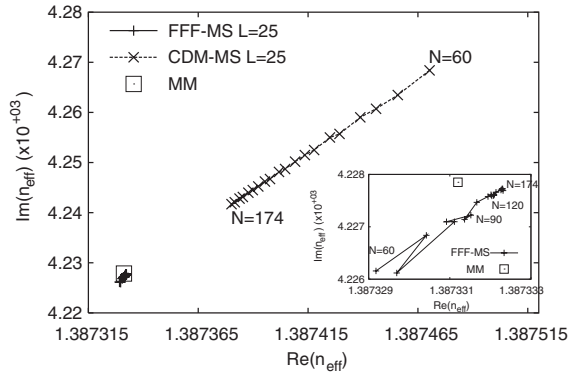

Figure 4. Convergence tests for the CDM-MS and FFF-MS versus the Fourier expansion order N for the effective index of the higher mode of symmetry class $p = 2$ with the highest effective index real part. The studied MOF is the six-hole test MOF described in the text. Inset: zoom of FFF-MS results and MM value.

gives $n_{eff} = 1.421\,0361 + i\,2.380\,70 \times 10^{-5}$ for $M = 12$ at $\lambda = 1.56$ μm. In this case, the FFF-MS gives $n_{eff} = 1.421\,035\,06 + i\,2.364\,53 \times 10^{-5}$ for $N = 60$ and $L = 45$ and $n_{eff} = 1.421\,036\,081 + i\,2.379\,84 \times 10^{-5}$ for $N = 150$ and $L = 105$. Consequently, the relative error is 1.3×10^{-6} for the real part of the effective index and 6.8×10^{-3} for the imaginary part for the first set of convergence parameters, and the relative error decreases to 1.3×10^{-8} for the real part of n_{eff} and to 3.6×10^{-4} for its imaginary part for the second set of parameters.

For a three-ring MOF at the same wavelength, the MM gives $n_{eff} = 1.421\,0465 + i\,8.118 \times 10^{-7}$ for $M = 12$ whereas the FFF-MS gives $n_{eff} = 1.421\,0445 + i\,7.928 \times 10^{-7}$ for $N = 60$ and $L = 70$ and $n_{eff} = 1.421\,0465 + i\,8.117 \times 10^{-7}$ for $N = 150$ and $L = 160$. The L values have been chosen in order to describe each inclusion layer, in the two MOFs, with the same number of layers in the S-algorithm. The relative error on the effective index is 1.4×10^{-6} for the real part and 2.3×10^{-2} for the imaginary part for the first set of convergence parameters, and the relative error decreases to 1.1×10^{-8} for the real part, and to 1.7×10^{-3} for the imaginary part for the second set of parameters.

We can conclude that the FFF-MS is now able to find accurately the effective indices of MOFs made of several rings
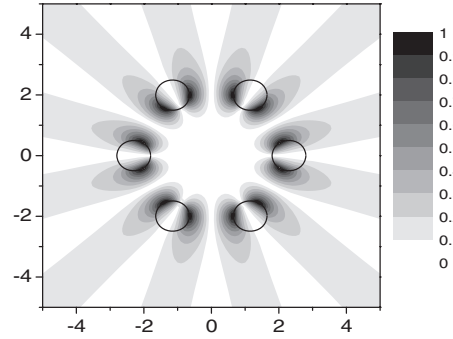
Figure 5. Modulus of electric field, in the core region for the higher order mode of symmetry class $p = 2$ with the highest effective index real part, $n_{eff} = 1.387\,329\,18 + i\,4.226\,16 \times 10^{-3}$ for $N = 60$. The field modulus is normalized to unity.

of inclusions. It is worth mentioning that three-ring MOFs are not only academic test fibres but also fabricated fibres as shown in [23].

As shown theoretically in the previous sections, the FFF-MS is also able to deal with the other symmetry classes. As an example we give the results for two higher order modes of our test MOF. The first one we consider belongs to symmetry class $p = 2$. The effective index obtained with the MM for $M = 12$ is $1.387\,3312 + i\,4.227\,8502 \times 10^{-3}$, whereas with the FFF-MS we obtained a value of $1.387\,329\,18 + i\,4.226\,16 \times 10^{-3}$ for $N = 60$. The convergence test for the FFF-MS is shown in figure 4 and the computed field map of this mode is depicted in figure 5. The third mode we study belongs to symmetry class $p = 1$. The effective index found with the MM for $M = 12$ is $1.388\,9179 + i\,5.761\,8884 \times 10^{-3}$, with the FFF-MS we obtained a value of $1.388\,914\,64 + i\,5.759\,47 \times 10^{-3}$ for $N = 60$. We can identify two properties when we compare the results for these two modes (see figure 6). First, for both modes the convergence of the FFF-MS is much faster than that of the CDM-MS. Second, the CDM-MS convergence is slower for the $p = 1$ mode (TM like) than for the $p = 2$ mode (TE-like), and this is not the case for the FFF-MS results (note the logarithmic y scale). These properties clearly illustrate the improvement ensured by the FFF, this recent method being initially proposed to solve the convergence problem of the CDM in diffraction studies for the TM polarization case [11].

Table 3. Comparison between the FFF-MS and the MM for the first modes of each symmetry class of the C_{6v} MOF described in the text. The results are computed at $\lambda = 1.56 \ \mu$m. For the MM the number of Fourier–Bessel coefficients is equal to 12, for the FFF-MS the number N of Fourier coefficients is set to 162. The relative error is computed from the normalized modulus of the difference between the two effective index values. Symmetry classes 3 and 4 are degenerate; so are classes 5 and 6.

Mode class	MM Re(n_{eff})	MM Im(n_{eff})	FFF-MS Re(n_{eff})	FFF-MS Im(n_{eff})	Relative error on Re(n_{eff})	Relative error on Im(n_{eff})
1	1.388 917 884	$5.761\,8884 \times 10^{-3}$	1.388 918 390	$5.761\,6371 \times 10^{-3}$	3.6×10^{-7}	4.4×10^{-5}
2	1.387 331 199	$4.227\,8502 \times 10^{-3}$	1.387 332 286	$4.227\,7231 \times 10^{-3}$	7.8×10^{-7}	3.0×10^{-5}
3, 4	1.420 784 521	$7.209\,5221 \times 10^{-4}$	1.420 784 943	$7.209\,4414 \times 10^{-4}$	3.0×10^{-7}	1.1×10^{-5}
5, 6	1.386 872 247	$5.037\,6883 \times 10^{-3}$	1.386 873 053	$5.037\,4468 \times 10^{-3}$	5.8×10^{-7}	4.8×10^{-5}
7	1.332 197 539	$1.942\,9823 \times 10^{-2}$	1.332 198 974	$1.942\,8629 \times 10^{-2}$	1.1×10^{-6}	6.1×10^{-5}
8	1.351 325 880	$2.155\,3168 \times 10^{-2}$	1.351 326 338	$2.155\,2000 \times 10^{-2}$	4.0×10^{-7}	5.4×10^{-5}

Table 4. Computer resources needed, on the same computer, by the FFF-MS and the MM to compute the fundamental mode for different MOF profiles. Note that several MOF structures cannot be treated by the multipole method. The number of coefficients in the Fourier–Bessel expansion in the MM is equal to $(2M + 1)$, and the number of coefficients in the Fourier expansion in the FFF-MS is equal to $(2N + 1)$. The considered sectorial C_{3v} MOF is described in section 5 and the considered inhomogeneous C_{6v} MOF is described in section 6.

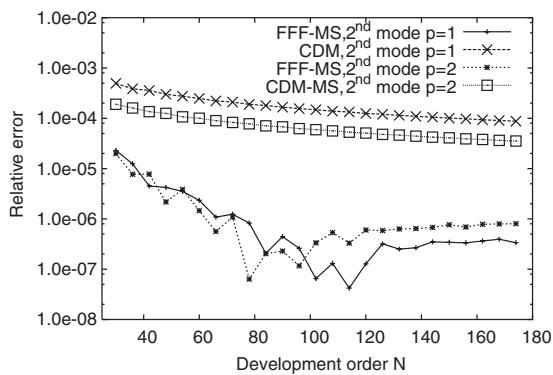| Configuration	MM time	MM RAM	FFF-MS time	FFF-MS RAM
Homogeneous C_{6v}	($M = 12$) 10 s	($M = 12$) 9 Mo	($N = 60$) 191 s ($N = 162$) 2700 s	($N = 60$) 16 Mo ($N = 162$) 50 Mo
Inhomogeneous C_{6v}	—	—	($N = 60$) 210 s	16 Mo
Sectorial C_{3v}	—	—	($N = 60$) 1062 s	16 Mo

Figure 6. Comparisons of the effective index relative error versus the Fourier expansion order N, for the higher modes of symmetry classes $p = 1$ and 2 with the highest effective index real part. The results for the FFF-MS and the CDM-MS are shown. The studied MOF is the six-hole test MOF described in the text.

Figure 7. Comparison between the FFF-MS (lines) and the MM (crosses) for the modal dispersion of the degenerate fundamental mode ($p = 3$ or 4) for the one- ($Nr = 1$) and two-ring ($Nr = 2$) C_{6v} MOFs described in the text, and for the modal dispersion of the second mode ($p = 2$) for the same one-ring MOF. For the MM the number of Fourier–Bessel coefficients is equal to 12, and for the FFF-MS N is set to 60.

In table 3 we recapitulate the comparisons between the effective indices obtained with the FFF-MS and the MM for the one-ring MOF. As can be seen, for all the possible mode classes of the C_{6v} MOF the FFF-MS provides accurate results. To complete the validation of the FFF-MS and to prove its usefulness in MOF studies, we also compare the modal dispersion computed with the two numerical methods for the fundamental mode of the two-ring MOF already studied. As can be seen in figure 7, the agreement between the two methods is excellent both for the real part and the imaginary part of the effective index.

In table 4, we give the resources needed on the same computer by the MM and the FFF-MS in order to find the fundamental mode of several MOF configurations. As expected, the MM is much more rapid than the FFF-MS since the MM involves fewer numerical computations. Nevertheless,
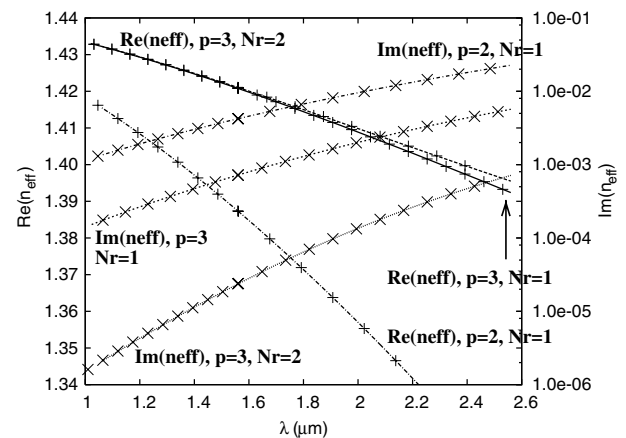
it can be seen that for complex structures which are not treatable by the MM the duration and the memory required by the FFF-MS are similar to the ones it requires for the C_{6v} homogeneous case. It is also worth mentioning that the program for the MM has been optimized several times from its first version in 2001; this is not yet the case for the FFF-MS program which is a recent one. This difference may enhance the gap due to the methods themselves seen in the computational durations observed in table 4.

4.2. A C_{2v} six-hole MOF

To conclude our tests of the FFF-MS method and its numerical implementation for calculating leaky modes in MOFs, we now

Table 5. Comparison between the FFF-MS, the FDM-ABC and the FEM-TBC for the effective index of the fundamental mode of the one-ring C_{3v} MOF described in the text.

n_{eff}	Degenerate fundamental mode ($p = 3, 4$)	Second mode ($p = 2$)
FDM-ABC	$1.355\,84 + \text{i}5 \times 10^{-5}$	$1.239\,57 + \text{i}5.09 \times 10^{-4}$
FEM-TBC	($p = 3$) $1.355\,81 + \text{i}4.96 \times 10^{-5}$	$1.239\,50 + \text{i}5.67 \times 10^{-4}$
	($p = 4$) $1.355\,80 + \text{i}4.95 \times 10^{-5}$	
FFF-MS $N = 60$	$1.355\,8867 + \text{i}5.012 \times 10^{-5}$	$1.239\,615 + \text{i}5.138 \times 10^{-4}$
FFF-MS $N = 150$	$1.355\,8863 + \text{i}5.011 \times 10^{-5}$	$1.239\,619 + \text{i}5.140 \times 10^{-4}$

consider a C_{2v} six-hole MOF similar to the one described in [2]. The MOF profile is a C_{2v} six-hole MOF with two types of holes. The pitch $\Lambda = 2.3\ \mu$m and the diameter of the four small holes is set to 1 μm and two symmetrically positioned small holes are now big holes of diameters equal to 1.4 μm. Due to their symmetry, there are only four symmetry classes (instead of eight in the C_{6v} case), none of them being degenerate [2]. Two core localized modes without nodes can be identified with the fundamental modes of the fibre; they belong respectively to symmetry classes $p = 3$ and 4. The real part for the effective index of this $p = 4$ mode is bigger than that of the $p = 3$ mode, whereas it is the contrary for the imaginary part. With the FFF-MS for $N = 60$, we obtain $n_{\text{eff}}(p = 3) = 1.417\,922\,19 + \text{i}5.111\,04 \times 10^{-4}$ and $n_{\text{eff}}(p = 4) = 1.418\,455\,87 + \text{i}5.275\,61 \times 10^{-4}$ instead of $n_{\text{eff}}(p = 3) = 1.417\,9265 + \text{i}5.114\,57 \times 10^{-4}$ and $n_{\text{eff}}(p = 4) = 1.418\,460 + \text{i}5.278\,45 \times 10^{-4}$ with the MM for $M = 12$. The good agreement between these results clearly shows that the FFF-MS can deal with other symmetries than the usual C_{6v} one, and can still reach a high accuracy.

5. Sectorial MOFs

To illustrate the capabilities of the FFF-MS to study the modal properties of MOFs with arbitrary profiles that are not treatable by the multipole method, extended [10] or not, we now describe some properties of sectorial MOFs. This type of MOF can be encountered when an extrusion process is used to build the fibre instead of the more conventional stack and draw technique [24, 25].

This structure with sectorial inclusions described in cylindrical coordinates is similar to lamellar gratings in Cartesian coordinates [11] since the cross-section profile is invariant according to the integration variable r (the lamellar grating profile is invariant according to the integration variable commonly chosen as y). For both cases, the Q_ϵ-matrix (see equation (1) and [13]) is independent of the integration variable (r or y). In addition, the integration matrix M also becomes independent of y for lamellar gratings. In this case, the rigorous coupled-wave (RCW) method is preferentially used (see chapter 6 in [11] and also [26]): the solutions of the differential set are explicitly known through to the eigenvalues and eigenvectors of the integration matrix. In contrast, the RCW method cannot be used in cylindrical coordinates with sectorial inclusions since the integration matrix $M(r)$ remains dependent on r owing to the terms $\frac{1}{r}$ and $\frac{1}{r^2}$ (see equations (7)–(9) in [14]). Consequently, the staircase approximation [27], which is based on the use of the RCW method, cannot be used. Nevertheless, for sectorial inclusions, the θ component of the normal vector to the inclusion surface is equal to unity along a

radial axis of the modulated area: $r \in [R_{\min}, R_{\max}]$, $[\![n_r^2]\!] = I_d$ and $[\![n_\theta^2]\!] = [\![n_\theta n_r]\!] = 0$. This property allows us to reduce the matrix Q_ϵ to

$$Q_\epsilon = \begin{bmatrix} [\![\epsilon]\!] & 0 & 0 \\ 0 & [\![\frac{1}{\epsilon}]\!]^{-1} & 0 \\ 0 & 0 & [\![\epsilon]\!] \end{bmatrix}. \qquad (21)$$

This matrix clearly illustrates the use of the inverse factorization rules [15] on the normal component of $\mathbf{D}$ to the considered surface, i.e. D_θ. The one-ring C_{nv} sectorial MOF geometry is described by the following geometric parameters: θ_m, the angle associated with one sector, $R_{\min}$, the minimum sector radius, $R_{\max}$, the maximum sector radius, and n, the number of sectors. We start with the last validation test of our method: a C_{3v} sectorial MOF studied in [28]. We choose this example because the inclusions are not circular and it illustrates symmetry properties not yet described in the previous sections of the present work. It also has the advantage that the results (table 2 in [28]) are obtained with two different methods: a finite element method with transparent boundary conditions (FEM-TBC) and a Fourier decomposition method with adjustable boundary conditions (FDM-ABC) [4]. The sectorial MOF parameters are $\lambda = 1.55\ \mu$m, $R_{\min} = 1\ \mu$m, $R_{\max} = 2\ \mu$m, $\theta_m = 54°$, $n_{\text{matrix}} = 1$ and $n_{\text{sector}} = 1.444\,023\,62$.

As can be seen from table 5, the variation of the real part of n_{eff} for the fundamental mode of the one-ring C_{3v} MOF between $N = 60$ and 150 is equal to 4×10^{-7} and the three methods give quite similar results. The extent of the modulated area is 1 μm, as in the C_{6v} one-ring MOF studied in section 4.1, and the wavelength is also similar. Besides, as pointed out in the previous paragraph, sectorial inclusions allow us to use the simpler expression given by equation (21) for the matrix Q_ϵ than the one used for circular inclusions. Hence we can expect that the accuracy of the computed results of this sectorial MOF for $N = 150$ is at least equal to the one obtained for the circular inclusion MOF, i.e. around 3×10^{-7} for the real part of n_{eff}. We can use a similar argument for the imaginary part. Consequently, the accuracy obtained with the FFF-MS is better than that given with the FDM-ABC and the FEM-TBC in [28]. We also notice that the degeneracy of the fundamental mode, theoretically predicted for C_{3v} structures by McIsaac's work [17], is obtained directly by the formalism detailed in section 3 for the FFF-MS, unlike for the FEM-TBC, in which a non-degenerate fundamental mode is found (see table 5). The field maps computed with the FFF-MS for the longitudinal component of the electric field are shown in figure 8. As shown by the theory the irreducible geometric angular sector where simple Dirichlet boundary conditions apply for this field component, for symmetry classes $p = 3$ or 4, is π and not $\pi/3$.

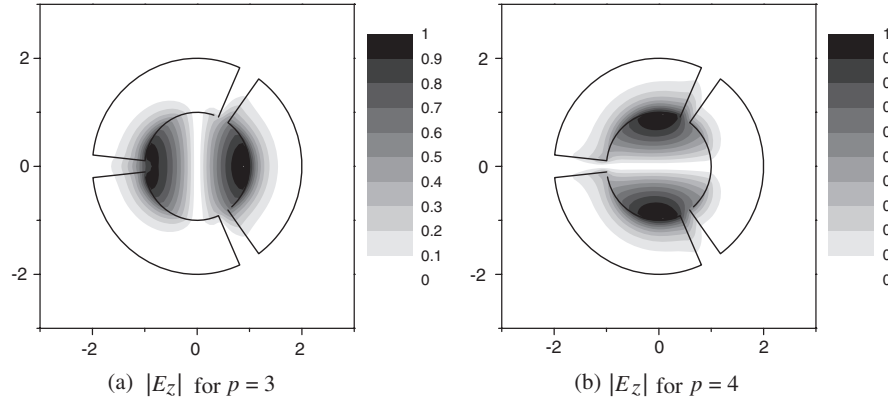(a) $|E_z|$ for $p = 3$

(b) $|E_z|$ for $p = 4$

Figure 8. Moduli of electric field longitudinal component of the C_{3v} sectorial MOF described in the text for the degenerate fundamental mode, for symmetry classes $p = 3$ and 4, $n_{eff} = 1.355\,8863 + i5.011 \times 10^{-5}$ for $N = 150$. The field moduli are normalized to unity.
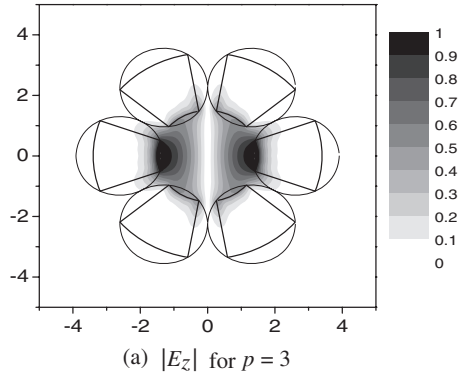

(a) $|E_z|$ for $p = 3$

Figure 9. Modulus of electric field longitudinal components for the degenerate fundamental mode which belongs to the symmetry classes $p = 3$ for the C_{6v} sectorial MOF ($R_{min} = 1.5\ \mu$m, $R_{max} = 3.4\ \mu$m and $\theta_m = 40°$), $n_{eff} = 1.403\,2977 + i\,2.9369 \times 10^{-6}$ for $N = 60$ and $L = 25$. The field moduli are normalized to unity. The thin circles correspond to the theoretical upper bound of the circle diameters for the MM.

Figure 10. Convergence test for the effective index of the fundamental mode of the six-sectorial-inclusion MOF ($R_{min} = 1.8\ \mu$m, $R_{max} = 2.8\ \mu$m, and $\theta_m = 19.5652°$) versus the Fourier expansion order N. The step in N is equal to 6. The number of slices in the S-algorithm L is set to 25.

Part of the cross-section of a six-sectorial-cylinder MOF is depicted in figure 9. We start our study by a MOF of this type with the same air filling fraction as the test example MOF we described in section 4.1. We have $R_{min} = 1.8\ \mu$m, $R_{max} = 2.8\ \mu$m, and $\theta_m = 19.5652°$. In this case, the effective index value is quite similar to the one already computed with the six-circular-hole MOF: we find $n_{eff} = 1.420\,506\,42 + i7.6390 \times 10^{-4}$ for $N = 60$. For $N = 120$, our search algorithm finds $n_{eff} = 1.420\,508\,87 + i7.6427 \times 10^{-4}$ for the fundamental mode of this sectorial MOF. Figure 10 shows the convergence test for this structure. The small loops which appear in the curve are not yet explained but they might be linked to the field expansions.

Going back to figure 9, we show the field map of the fundamental mode of a six-sectorial-cylinder MOF that cannot be studied even with an extended version of the MM since the circles which include the inclusions are tangent. Mode searching in such structure is straightforward with the FFF-MS and does not require special treatment.

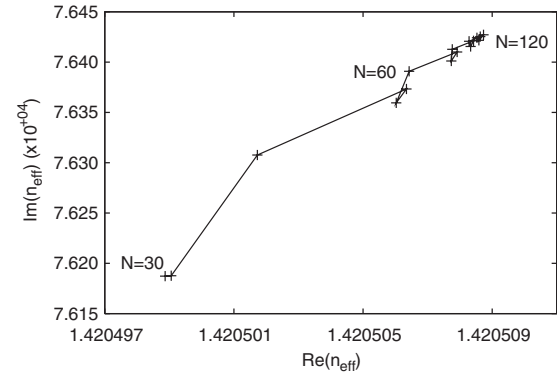In figure 11, we give the trajectory in the complex plane of the sectorial MOF fundamental mode effective index as a function of its geometrical parameters. The decrease of the inner radius a induces an important decrease of $Re(n_{eff})$ without any significant change in the losses. This can be qualitatively understood as follows: the fields tend to spread over the low-index inclusions, lowering the effective index. In contrast, the increase of the outer radius b induces a fall in the losses, keeping nearly constant the real part of n_{eff}. This behaviour can also be explained; the change on the structure does not modify the inner part of the confining region which controls the field shape and so consequently $Re(n_{eff})$, but this change isolates more deeply the fibre core from the outside region, reducing strongly $Im(n_{eff})$. The increase of the angle θ_m implies a decrease of both the real and the imaginary parts of n_{eff}. We can again explain this quite simply: this change alters the inner shape of the core through an increase of the low-index region inducing a decrease of $Re(n_{eff})$, and at the same time it isolates the core from the outside (decrease of $Im(n_{eff})$).

6. Inhomogeneous MOFs

In this penultimate section, we illustrate the capability of the FFF-MS to deal with inhomogeneous inclusions. We start with
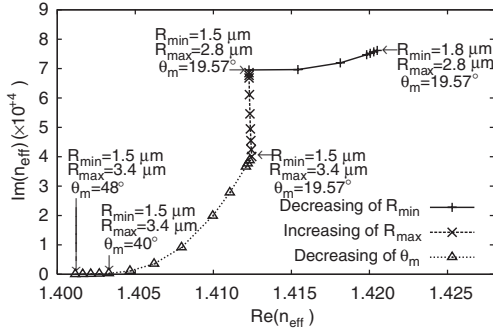
Figure 11. Evolution of the effective index n_{eff} as a function of the three geometrical parameters a, b and θ_m describing the C_{6v} sectorial MOF. The labels are written for the extremal values of the parameters.
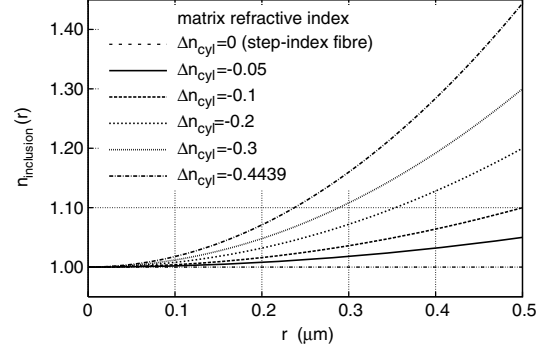

Figure 12. Chosen parabolic profile of the inhomogeneous inclusions for several values of the refractive index gap Δn_{cyl} between the inclusion centre and the inclusion outer boundary. The analytic form of the refractive index profile is given in the text.

a validation study using a single high index cylinder with a parabolic refractive index profile in a homogeneous matrix. Then we study a MOF made of six inhomogeneous inclusions.

The first device is studied with two different algorithms. The first one considers an inhomogeneous circular cylinder centred at the coordinate origin and does not use the FFF-MS but a semi-analytical calculus detailed below. In order to model a fibre with an inhomogeneous radial index profile which is centred at the origin, the interior region of this fibre is split (in the same way as the modulated area in the S-matrix propagation algorithm) into P homogeneous layers. For each homogeneous layer (p) with $p \in [1, P]$ between the two circular cylinders with radius r_p and r_{p+1}, the corresponding refractive index is chosen as the average of the parabolic index profile between r_p and r_{p+1}. The higher the P value, the better the index profile is described, and the transmission matrix of all the P layers becomes the product of the P transmission matrices of the homogeneous layers. In fact, the transmission matrix (and the S-matrix) of a layer between two circular cylinders centred at the origin and filled with a homogeneous medium may be deduced directly from the explicit expressions of the fields in such a medium (with the $\Psi^{(j)}(r)$-matrix in equation (34) of [13]) by writing the continuity of the fields at each interface. So, no integration is required and the differential set (2) is not used.

It is important to distinguish the present splitting of a radially inhomogeneous circular cylinder into P slices from the moot procedure invoking the staircase approximation [27]. With this last method, the arbitrary diffracting surface is split into several lamellar diffracting surfaces. However, the discretization of the smooth profile in a staircase form introduces edges leading to diverging fields and thus worsening the convergence rate. In our case, there is no diffracting surface but only fictitious surfaces created at the interfaces of the homogeneous layers. In other words, the splitting concerns the index profile and not a diffracting surface.

The second algorithm deals with the same inhomogeneous fibre but not centred at the coordinate origin, and it uses the complete FFF-MS described in the present work: the differential set (2) must be integrated numerically.

To describe the refractive index profile of both the test fibre of this paragraph and the MOF we consider below we write for $r \in [0, r_{max}]$: $n(r) = n_{cyl,cent} - (n_{cyl,cent} -$

$n_{cyl,bord})(r/r_{max})^2$, in which $n_{cyl,cent}$ is the refractive index at the inclusion centre and $n_{cyl,bord}$ the refractive index at the inclusion boundary ($r = r_{max}$). For the test fibre we set: radius $r_{max} = 0.5$ μm, $n_{cyl,cent} = 1.5$, $n_{cyl,bord} = n_{mat} = 1.47$, $\lambda = 0.4$ μm, $n(r) = n_{cyl} - (n_{cyl} - n_{mat})(r/r_{max})^2$. For the fundamental mode HE_{11}, an approximate semi-analytical solution associated with an infinite parabolic profile is known [29]. It gives for the approximate effective index value $n_{eff} = 1.48727747$. It is important to notice that in the special case in which the centre of the fibre corresponds to the coordinate origin we can use the first algorithm described at the beginning of this section. In this case, we obtain $n_{eff} = 1.48727514$ for $N = 1$ and $P = 200$. This accurate value will be our reference value for the next test. In order to validate the second algorithm associated with the FFF, we study the same inhomogeneous fibre but not centred at the origin (we set the fibre centre position such that $R_{centre} = 3$ μm). In this case, the symmetry is broken; thus more Fourier coefficients are needed to correctly describe the fields and we must use the algorithm of the FFF. The convergence is easily reached in this example; we obtain $n_{eff} = 1.48727382$ for $N = 30$ and $L = 50$.

The MOF model we consider now is the one-ring MOF already described in section 4.1, but in the present case the refractive index profile of each inclusion follows a radial parabolic law. We recall that in the type of MOFs studied the inclusion refractive index is lower than that of the matrix (in the previous paragraph the isolated fibre has a higher refractive index than the matrix one). We introduce $\Delta n_{cyl} = (n_{cyl,cent} - n_{cyl,bord})$, the refractive index gap of the inclusions (not the gap between the inclusion and the matrix indices). These parabolic profiles are depicted in figure 12. We may discuss the accuracy of the results according to the expansion order N, and to the number of integration steps (and the number of S-slices L). In the case of the homogeneous inclusions, we know that the higher the N value, the better the discontinuities of the ϵ, n_θ^2, n_r^2 and $n_\theta n_r$ functions are described according to θ. In the same way, the higher the number of integration steps, the better the radial refractive index profile is defined along a radial axis. For inhomogeneous inclusions in a matrix such that $n_{cyl,bord} = n_{mat}$, the refractive index profile becomes continuous in the whole space. This property explains why, in this case, the Gibbs phenomenon due
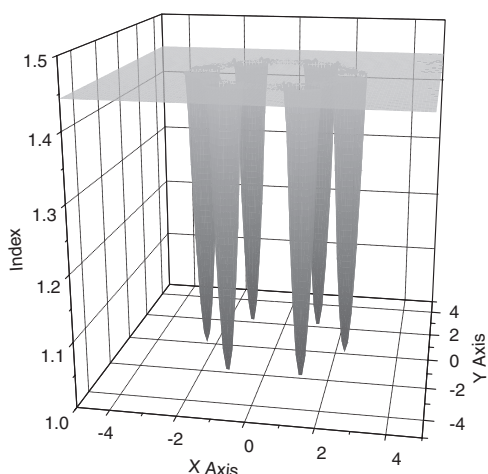
Figure 13. Refractive index profile of the one-ring C_{6v} inhomogeneous MOF described in the text; this profile is rebuilt from the Fourier series of the theoretical parabolic profile with $n_{cyl,bord} = n_{mat}$.

Figure 14. Effective index of the fundamental mode for the one-ring C_{6v} inhomogeneous MOF according to the inclusion refractive index gap Δn_{cyl}, for $\Delta n_{cyl} = 0$ we recover homogeneous inclusions (see the text and figures 12 and 13).

to discontinuities with respect to θ does not occur. However, the shape of the parabolic refractive index profile requires more Fourier coefficients (higher value of N) but also more integration steps according to r, in order to describe accurately the structure compared to a homogeneous profile. For these reasons, we have observed that the accuracies obtained for a MOF with inhomogeneous inclusions but continuous refractive index profile remains of the same order of magnitude as those of a similar MOF with homogeneous inclusions when the N and L values are identical. In figure 13, we show the rebuilt profile of the whole MOF from the Fourier series used in the FFF-MS and not the theoretical profile. As can be seen, the resulting profile is regular, and fits well the parabolic law. In figure 14, we give the computed effective indices of the fundamental mode for the inclusion parabolic profiles described in figure 12. As expected, both the real part and the imaginary part of the effective indices decrease when Δn_{cyl} increases up to zero.

7. Conclusion

Thanks to various and complete comparisons with the well established multipole method and with more recent numerical methods, we can state that the FFF-MS, a mode searching method based on the differential method with the fast Fourier factorization, can find the different modes of solid core MOFs with a high accuracy both for the real part and the imaginary part of the effective index. This method can deal with both the fundamental mode and higher order modes. It can study arbitrary refractive index profile MOFs in contrast to the multipole method. New results are given for C_{6v} sectorial MOFs and inhomogeneous MOFs. The counterpoints to the versatility of the developed method are its lower accuracy, which however is largely sufficient to compute accurately the modal dispersion, and its need for larger computer resources compared to the multipole method.

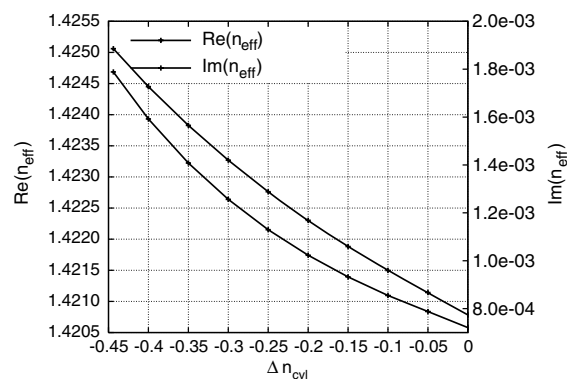In the case of a profile periodic according to the angular variable, the symmetry properties of the modes are established, not in the real space as for the MM, but in Fourier space. The results given are valid for all waveguides fulfilling C_{nv} symmetries and can be easily extended to C_n waveguides, not just MOFs, and apply to all differential methods formulated using cylindrical coordinates (not just the FFF). These results allow both a clear mode classification and a large reduction of the necessary computational resources.

In future work we plan to analyse the properties of anisotropic (longitudinal/transverse relative permittivities induced by liquid crystals for example) MOFs since the differential method with the fast Fourier factorization is also able to deal with such structures even if the matrix which links **D** and **E** becomes more complicated.

References

[1] White T P, Kuhlmey B, McPhedran R C, Maystre D, Renversez G, Martijn de Sterke C and Botten L C 2002 Multipole method for microstructured optical fibers I: formulation *J. Opt. Soc. Am.* B **10** 2322–30
[2] Zolla F, Renversez G, Nicolet A, Kuhlmey B, Guenneau S and Felbacq D 2005 *Foundations of Photonic Crystal Fibres* (London: Imperial College Press)
[3] Brechet F, Marcou J, Pagnoux D and Roy P 2000 Complete analysis of the characteristics of propagation into photonic crystal fibers by the finite element method *Opt. Fiber Technol.* **6** 181–91
[4] Issa N A and Poladian L 2003 Vector wave expansion method for leaky modes of microstructured optical fibers *J. Lightwave Technol.* **21** 1005–12
[5] Saitoh K and Koshiba M 2003 Leakage loss and group velocity dispersion in air–core photonic bandgap fibers *Opt. Express* **11** 3100–9
[6] Kuhlmey B, White T P, Renversez G, Maystre D, Botten L C, de Sterke C M and McPhedran R C 2002 Multipole method for microstructured optical fibers II: implementation and results *J. Opt. Soc. Am.* B **10** 2331–40

[7] Kuhlmey B, Renversez G and Maystre D 2003 Chromatic dispersion and losses of microstructured optical fiber *Appl. Opt.* **42** 634–9

[8] Kuhlmey B, McPhedran R C and de Sterke C M 2002 Modal 'cutoff' in microstructured optical fibers *Opt. Lett.* **27** 1684–6

[9] Renversez G, Bordas F and Kuhlmey B T 2005 Second mode transition in microstructured optical fibers: determination of the critical geometrical parameter and study of the matrix refractive index and effects of cladding size *Opt. Lett.* **30** 1264–6

[10] Campbell S, McPhedran R C, de Sterke C M and Botten L C 2004 Differential multipole method for microstructured optical fibers *J. Opt. Soc. Am.* B **21** 1919–28

[11] Nevière M and Popov E 2003 *Light Propagation in Periodic Media* (New York: Dekker)

[12] Boyer P, Popov E, Nevière M and Tayeb G 2004 Diffraction theory in TM polarization: application of the fast Fourier factorization method to cylindrical devices with arbitrary cross section *J. Opt. Soc. Am.* A **21** 2146–53

[13] Boyer P, Nevière M, Popov E and Renversez G 2006 Diffraction theory: application of the fast Fourier factorization method to cylindrical devices with arbitrary cross section lighted in conical mounting *J. Opt. Soc. Am.* A **23** 1146–58

[14] Boyer P, Renversez G, Popov E and Nevière M 2006 A new differential method applied to the study of arbitrary cross section microstructured optical fibers *Opt. Quantum Electron.* **38** 217–30

[15] Li L 1996 Use of Fourier series in the analysis of discontinuous periodic structures *J. Opt. Soc. Am.* A **13** 1870–6

[16] Golub G H and Van Loan C F 1996 *Matrix Computations* 3rd edn (Baltimore and London: John Hopkins University Press)

[17] McIsaac P R 1975 Symmetry-induced modal characteristics of uniform waveguides-I: summary of results *IEEE Trans. Microw. Theory Tech.* **23** 421–9

[18] McIsaac P R 1975 Symmetry-induced modal characteristics of uniform waveguides-II: theory *IEEE Trans. Microw. Theory Tech.* **23** 429–33

[19] Fini J M 2004 Improved symmetry analysis of many-moded microstructure optical fibers *J. Opt. Soc. Am.* B **21** 1431–6

[20] Bai B and Li L 2004 Reduction of computation time for crossed-grating problems: a group-theoretic approach *J. Opt. Soc. Am.* A **21** 1886–94

[21] Bai B and Li L 2005 Group-theoretic approach to the enhancement of the Fourier modal method for crossed gratings: C_2 symmetry case *J. Opt. Soc. Am.* A **22** 654–61

[22] Vincent P and Petit R 1972 Sur la diffraction d'une onde plane par un cylindre diélectrique *Opt. Commun.* **5** 261–6

[23] Brilland L, Smektala F, Renversez G, Chartier T, Troles J, Nguyen T, Traynor N and Monteville A 2006 Fabrication of complex structures of holey fibers in chalcogenide glass *Opt. Express* **14** 1280–5

[24] Kiang K M, Frampton K, Monro T M, Moore R, Tucknott J, Newak D W, Richardson D J and Rutt H N 2002 Extruded single-mode non-silica glass holey optical fibres *Electron. Lett.* **38** 546–7

[25] Ravi Kanth Kumar V V, George A K, Reeves W H, Knight J C, Russell P St, Omenetto F G and Taylor A J 2002 Extruded soft glass photonic crystal fiber for ultrabroad supercontinuum generation *Opt. Express* **10** 1520–4

[26] Peng S T, Tamir T and Bertoni H L 1975 Theory of periodic dielectric waveguides *IEEE Trans. Microw. Theory Tech.* **23** 123–33

[27] Popov E, Nevière M, Gralak B and Tayeb G 2002 Staircase approximation validity for arbitrary shaped gratings *J. Opt. Soc. Am.* A **19** 33–42

[28] Uranus H P and Hoekstra H J W M 2004 Modelling of microstructured waveguides using a finite-element-based vectorial mode solver with transparent boundary conditions *Opt. Express* **12** (12)

[29] Snyder A W and Love J D 1983 *Optical Waveguide Theory* (New York: Chapman and Hall)